

Characterization of the optical and X-ray properties of the northwestern wisps in the Crab Nebula

T. Schweizer^{1*}, N. Bucciantini^{2,6}, W. Idec^{1,7}, K. Nilsson³, A. Tennant⁴
M.C. Weisskopf⁴ and R. Zanin⁵

¹Max-Planck-Institute for Physics, Foehringer Ring 6, 80805 Munich, Germany

²INAF - Osservatorio Astrofisico di Arcetri, L.go E. Fermi 5, 50125, Firenze, Italy

³Finnish Centre for Astronomy with ESO (FINCA), University of Turku, 20, FI-21500, Finland

⁴Space Science Department, NASA Marshall Space Flight Center, ZP12, Huntsville, AL 35812

⁵Universitat de Barcelona, Departament d'Astronomia i Meteorologia, Spain

⁶INFN - Sezione di Firenze, Via G. Sansone 1, 50019 Sesto Fiorentino, Firenze, Italy

⁷Department of Astrophysics, University of Łódź, ul. Pomorska 149/153, 90-236 Łódź, Poland

ABSTRACT

We have studied the wisps to the northwest of the Crab pulsar as part of a multi-wavelength campaign in the visible and in X-rays. Optical observations were obtained using the Nordic Optical Telescope in La Palma and X-ray observations were made with the Chandra X-ray Observatory. The observing campaign took place from October 2010 until September 2012. About once per year we observe wisps forming and peeling off from (or near) the region commonly associated with the termination shock of the pulsar wind. We find that the exact locations of the northwestern wisps in the optical and in X-rays are similar but not coincident, with X-ray wisps preferentially located closer to the pulsar. This suggests that the optical and X-ray wisps are not produced by the same particle distribution. Our measurements and their implications are interpreted in terms of a Doppler-boosted ring model that has its origin in MHD modeling. While the Doppler boosting factors inferred from the X-ray wisps are consistent with current MHD simulations of PWNe, the optical boosting factors are not, and typically exceed values from MHD simulations by about a factor of 4.

Key words: ISM: supernova remnants - pulsars: individual: Crab - radiation mechanisms: non-thermal - ISM: supernova remnants: individual: Crab Nebula

1 INTRODUCTION

The Crab Nebula is one of the most studied targets in the sky as it is bright and observable over a very broad spectral range. The Nebula is a remnant from a supernova explosion that was observed on earth in 1054 C.E. Located at a distance of ~ 2 kpc, the system is powered by a pulsar of spin-down luminosity $L \sim 5 \times 10^{38}$ erg s⁻¹ and period $P \sim 34$ ms. The history and general properties of the system are nicely summarized in the review by Hester (2008).

Amongst the most prominent features of the inner nebula are the oppositely-directed jets, a torus and a rich variable “wisp” structure (Scargle 1969) more prominent to the northwest than the southeast. In the past decade, there have been several detailed observations in various wavelengths that observed the jet, found a knot at the beginning of the jet close to the pulsar (about $0.7''$), and reconfirmed the wisps

(Hester et al. 1995; Bietenholz et al. 2004; Hester 2008). Observations with the Hubble Space telescope (HST) showed the the optical wisps form and dissipate over timescales of months (Hester et al. 2002). In addition, variable (in both position and time) X-ray-emitting knots also are present, especially to the southeast of the pulsar (Weisskopf et al. 2012).

The discovery of γ -ray flaring in 2010 September (Tavani et al. 2011; Abdo et al. 2011) stimulated a renewed interest in the Crab Nebula. Here we present the results of two observing campaigns, one in the visible and one in X-rays inspired by the search for the origin of the γ -ray flaring. In this paper we concentrate on characterizing the wisps to the northwest of the pulsar. As part of the campaign, we also obtained data during the γ -ray flaring activity of April 2011 (Buehler et al. 2012). However, we see no direct correlation between the appearance of either an optical or an X-ray wisp and the γ -ray flaring.

We describe the optical (§2.1) and X-ray (§2.2) obser-

* E-mail:tschweiz@googlemail.com

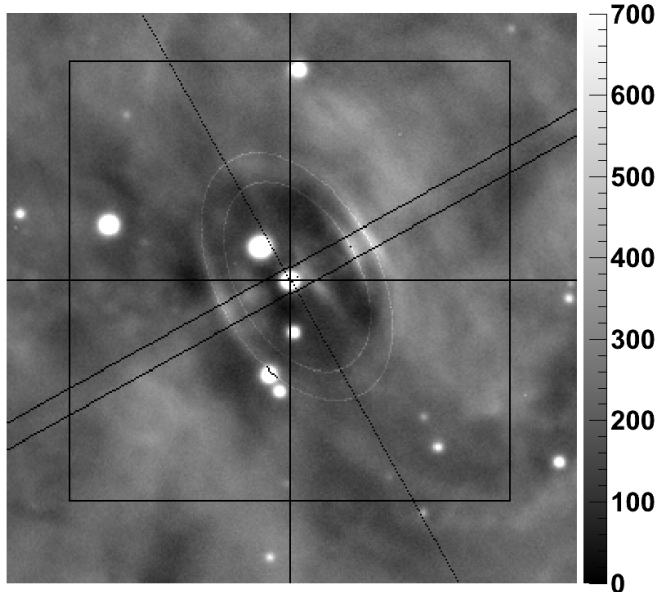


Figure 1. Optical image of the inner portion of the Crab Nebula taken on 13th of April 2011 and during a γ -ray flare (Buehler et al. 2012). North is up and east is to the left. The square covers a field of view of $50'' \times 50''$. The long, narrow rectangle at a position angle of 119° outlines the region used to measure the radial profile. Two ellipses are fitted to the two most prominent wisps at 8.0 arcsec and 10.1 arcsec distance from the pulsar. The ellipses have been anchored by fits to the peak positions in the northwest. The radial profiles of this image are shown in Fig. 3. The aspect ratio of the ellipses is 0.6 and the center of the ellipses are offset from the pulsar by $0.8''$ in the line of the pulsar and the peak emission of the wisps. Low frequency background has been removed from this image for better visibility. The units are arbitrary.

vations. Data reduction and derived physical parameters are presented as follows: wisp radial profiles (§3.1), wisp velocities (§3.2) and wisp azimuthal profiles (§3.3). In §4 we make use of a Doppler-boosted ring model to the observations and discuss implications. We briefly summarize our findings in §5.

2 THE OBSERVATIONS

2.1 The Optical Observations

Optical data was obtained using the 2.56m Nordic Optical Telescope (NOT) located in the Observatorio del Roque de los Muchachos on the Canary island La Palma. Altogether 24 images were taken from November 2010 until September 2012 using the Andalucia Faint Object Spectrograph and Camera (ALFOSC). The instrument employs a 2048×2048 E2V chip with a gain of $0.327e^-/\text{ADU}$, a readout noise of $4.2e^-$ and a scale of $0.19''/\text{pixel}$ giving a field of view of 6.5×6.5 arcmin. Two to four exposures of 200s - 300s were made through the I-band filter (NOT filter #12, λ_c around 800nm) at each epoch. The effective seeing resolution depends on observing conditions and ranges between $0.49''$ and $1.1''$. Table 1 lists the dates and seeing resolution for each optical observation.

The images were processed first by subtracting the aver-

Table 1. Optical observation dates and seeing resolution

MJD ^a	Date ^b	Seeing ^c
55518.1	2010/11/18	0.49
55532.0	2010/12/02	0.69
55557.9	2010/12/27	0.83
55564.1	2011/01/03	0.87
55570.0	2011/01/09	0.59
55598.8	2011/02/06	0.62
55612.9	2011/02/20	0.70
55647.9	2011/03/27	0.49
55664.9	2011/04/13	0.78
55810.2	2011/09/06	0.54
55863.2	2011/10/29	0.99
55881.1	2011/11/16	0.60
55922.1	2011/12/27	0.61
55954.9	2012/01/28	1.05
55986.9	2012/02/29	0.72
55998.9	2012/03/12	0.96
56013.9	2012/03/27	0.60
56025.9	2012/04/08	0.75
56033.9	2012/04/16	1.02
56140.2	2012/08/01	0.82
56141.2	2012/08/02	0.82
56153.2	2012/08/14	0.52
56159.2	2012/08/20	1.10
56176.2	2012/09/06	0.75

^a Modified Julian Date of start of observation.

^b UTC date.

^c Seeing FWHM in arcsec.

age bias image and then dividing by a twilight-sky flat-field image. The fringe pattern was removed using a fringe correction image created from archival NOT data taken using the same instrument configuration. After scaling and subtracting the fringe correction image, the fringe pattern was no longer visible. Individual frames were then registered using 8 stars in the vicinity of the pulsar and then averaged.

We checked the NOT plate scale using an Hubble Space Telescope (HST) legacy archive image of the Crab pulsar obtained with the Wide Field and Planetary Camera 2 (WFPC2) on Aug 14, 1995. Using the Planetary Camera (PC) portion of the image we selected two pairs of unsaturated stars within 25 arcsec of the pulsar and determined the distance between the two stars in each pair using the 0.05 arcsec/pix plate scale of the image. Measuring the distances of the same pairs in the NOT image we arrived at NOT plate scale of 0.1902 and 0.1904 arcsec/pix. Hence the adopted plate scale 0.19 arcsec/pix is expected to be accurate to within 0.2%.

Sky background was subtracted from the average frames by fitting two models to the “pure sky” regions around Crab: a constant and a low-order polynomial. The two methods generally agreed to better than 1.2% when extrapolated to the location of the pulsar. We use the constant in what follows. Flux calibration used the comparison star sequence given in Sandberg & Sollerman (2009). We used star 3 with I-band magnitude $I = 16.26 \pm 0.02$ from their calibration sequence to determine the zero point, ZP , by fitting a Point Spread Function (PSF) model created from star 1 of Sandberg & Sollerman (2009) to star 3. The conversion from sky-

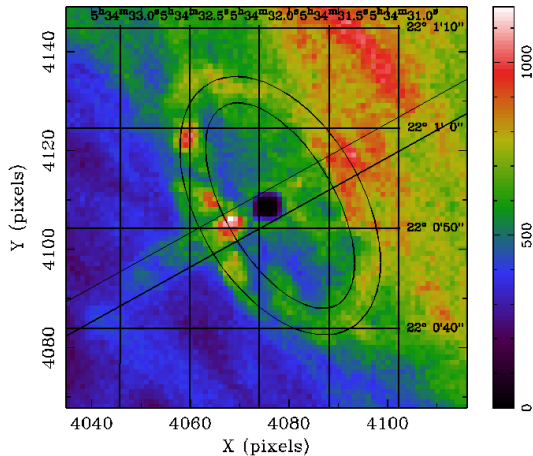


Figure 2. This Chandra X-ray image of the inner portion of the Crab Nebula is the sum of the observations from the 14th to the 28th of April 2011 during the γ -ray flare. The axes are ACIS detector pixels ($0.492''/\text{pixel}$). The best fitting ellipse of the wisp emission has an aspect ratio of 0.49 and an offset of $0.9''$ at a position angle of 110° (Weisskopf et al. 2012). The color scale is in counts. The black feature with zero counts is the burned out image of the pulsar. The color scale are photon counts per ACIS pixel in the 0.5-8 keV band.

subtracted counts, N (ADU), to physical fluxes, F (μJy per pixel), is then

$$F = 2550 * 10^{-0.4 * (ZP - 2.5 \log N)} \quad (1)$$

Since the calibration was obtained from a star in the Crab image, variations in atmospheric transparency are effectively accounted for and removed. To check the accuracy of the calibration we measured the total flux of a $5.9'' \times 7.8''$ wisp-free, rectangular region $\sim 40''$ east of the Pulsar and of apparent uniform surface brightness. The rms scatter of the flux from this region is 3.3% over the 24 observations. We ascribe most of this scatter to flat-fielding-, calibration- and background-determination errors as the expected scatter, considering only the photon noise and the readout noise, is $< 0.1\%$. Fig. 1 shows one of the 24 optical images.

2.2 The X-ray Observations

Subsequent to the discovery of γ -ray flaring in 2010 September (Tavani et al. 2011; Abdo et al. 2011) a series of Chandra X-ray Observatory observations was initiated on approximately a monthly cadence. Five Target of Opportunity observations were performed during the April 2011 γ -ray flare and the average of those 5 images is shown in Fig. 2. Chandra observations have continued, now as part of the Chandra general observer program, yielding a sequence which covers approximately two years. As with our optical observations, the coverage is not continuous, since Chandra is not allowed to point within 45° of the Sun. The solar restriction results in about a 90 day interval during the summer when the Crab may not be observed. A list the Chandra observations used for this paper is given in Table 2.

All data were taken with the back-illuminated ACIS-S3¹ detector at the focus of the telescope in the energy band 0.5-8 keV. Owing to the Crab's high flux, the observations were taken with the shortest possible frame time of 0.2s to minimize pileup. Even with this frame time, pileup impacts the brighter regions of the nebula. Telemetry saturation is also a issue with such a bright source, so we restricted data to a 300×300 ACIS-pixel ($\approx 150'' \times 150''$) region that covers the bright part of the nebula. The integration time was 5 ksec for monitoring observations and 10 ksec for the 5 observations following the 2011 April γ -ray flare. Due to telemetry saturation the effective exposure time was 600 or 1200s (Table 2).

For the first three observations (Table 2) the dither amplitude of the spacecraft was set to zero. Since pileup characteristics may be different if the pulsar image is at the middle, edge or corner of a pixel, we then used a small ($1''$ amplitude) dither for the remaining observations. This dither ensures the pulsar and other sharp features in the nebula are averaged over a few pixels.

Level 2 event files were created using the CIAO tool `acis_process_events` using the EDSEER option (Li et al. 2004) to improve the subpixel positioning. Due to severe pileup the pulsar does not appear in the image (Fig. 2). We did not simply rely on the Chandra aspect solution, but re-registered images making use of the readout trail (out-of-time image of the pulsar) to constrain one dimension and the burned out image of the pulsar to constrain the other coordinate.

Due to the different roll orientations of the Observatory, the readout trail could introduce some bias in the azimuthal distribution. We removed this trail by computing the average number of counts per pixel due to the trail. Then, based on the actual number of counts seen in a pixel and our estimate of the number due to the readout streak, we randomly rejected events. Since this method is statistical, it is not perfect, but it will remove the principal brightness peak in the data due to the trail itself.

3 DATA ANALYSIS

Images were analyzed to characterize the shape of the wisps in both the radial direction from the pulsar and angular extent about the pulsar. Our analysis to determine the radial distribution through the wisp restricted data to a slim elongated rectangle $3''$ in width at a position angle of 119° measured positive east of north. The rectangular region is shown in Figs. 1 and 2. Optical and X-ray data were binned in radial bins of $0.11''$ and $0.492''$ respectively. The analysis of azimuthal distributions utilized $0.5''$ -wide elliptical annuli, on the sky and centered on the peak of the radial distribution.

3.1 Analysis of the radial profile of the wisps

An example of an optical and an X-ray radial profile measured close in time is shown Fig. 3. We see two prominent peaks in the optical and the presence of at least three peaks

¹ <http://asc.harvard.edu/proposer/POG/> Chapter 6.

Table 2. Time-ordered list of Chandra observations with exposure time used for this paper.

ObsID ^a	MJD ^b	Date ^c	Time ^d
13139	55467.2	2010/09/28	600
13146	55497.7	2010/10/28	600
13147	55528.5	2010/11/28	600
13204	55576.0	2011/01/15	600
13205	55608.7	2011/02/16	600
13206	55635.2	2011/03/15	600
13207	55663.6	2011/04/12	600
13150	55665.0	2011/04/14	1200
13151	55665.6	2011/04/14	1200
13152	55667.4	2011/04/16	1200
13153	55673.0	2011/04/22	1200
13154	55679.3	2011/04/28	1200
13208	55788.4	2011/08/15	600
13209	55819.2	2011/09/15	600
13210	55849.2	2011/10/15	600
13750	55892.7	2011/11/27	600
13751	55938.1	2012/01/12	600
13752	55967.4	2012/02/10	600
14416	56005.3	2012/03/19	600
13754	56039.1	2012/04/22	600
13755	56155.6	2012/08/16	600
13756	56181.9	2012/09/11	600

^a Chandra observation identifier.^b Start of observation MJD.^c UTC date.^d Approximate effective exposure time in seconds.**Table 3.** Velocities of the wisps identified in Figs. 5 and 6.

symbol	" / day	(v/c) ^a	(v/c) ^b
Optical (red)			
circle	0.018	0.21	0.29
box solid	0.033	0.38	0.44
triangle up	0.021	0.24	0.32
triangle down	0.012	0.14	0.21
star	0.019	0.22	0.30
X-rays (blue)			
circle	0.014	0.16	0.24
box solid	0.017	0.19	0.28
box open	0.020	0.23	0.31
star solid	0.031	0.35	0.42
triangle up	0.024	0.28	0.36
triangle down	0.011	0.12	0.19
cross	0.009	0.10	0.16

^a Apparent velocity on the sky.^b Deprojected velocity.

in the X-ray profile. In general, the peak closest to the pulsar is most usually identified with the location of the termination shock. Fig. 3 demonstrates that the X-ray peak at 10'' is located at a slightly different (and smaller) distance than the peak in the optical.

Fig. 4 top is the radial profile of the average of all the optical observations. Notice the strong peak at 8'' showing

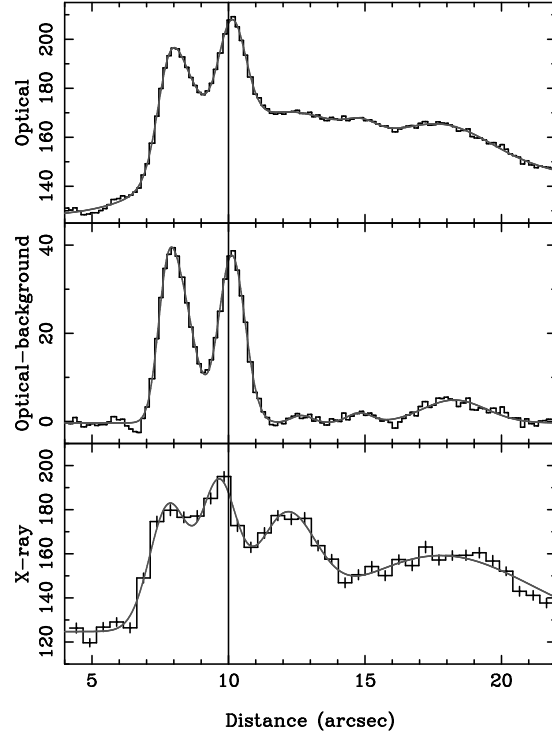


Figure 3. The upper panel shows the radial distribution for the optical data for April 13, 2011 (in units of $\mu\text{Jy}/\text{arcsec}^2$) and the bottom panel the X-ray radial distribution for the average from April 14 until April 28, 2011 (photon counts per ACIS pixel). The middle curve is the same as the uppermost curve but with low frequency terms subtracted. The solid lines are a model fit based on a number of Gaussians. The vertical at 10'' shows that the optical and X-ray peaks do not exactly coincide.

that the optical wisps are brightest at this distance and then fade at larger distances. Fig. 4 bottom shows the same plot in X-rays averaged with the same sampling interval as for the optical. The innermost X-ray arc, at $\sim 7.5''$, is brightest.

3.2 The radial evolution of the wisps as a function of time

Fig. 5 shows most of the optical and X-ray radial projections as a function of the angular distance from the pulsar along the position angle of 119° as a function of time. Low frequency terms (background) have been subtracted for better visibility. The algorithm applied was the TSpectrum::Background()-method from the ROOT-package (Morh c et al. 1997). In the figure we also trace the outward motion of a particular peak by drawing a line through the position of what appears to be the same peak but at different times. There appear to be possibly 5 distinct progressions of peaks in the optical data and possibly 7 in X-rays. We have not attempted to connect progressions across summer gaps, but one could do so. As the slopes of the lines indicating the outward progression are different, so are the inferred

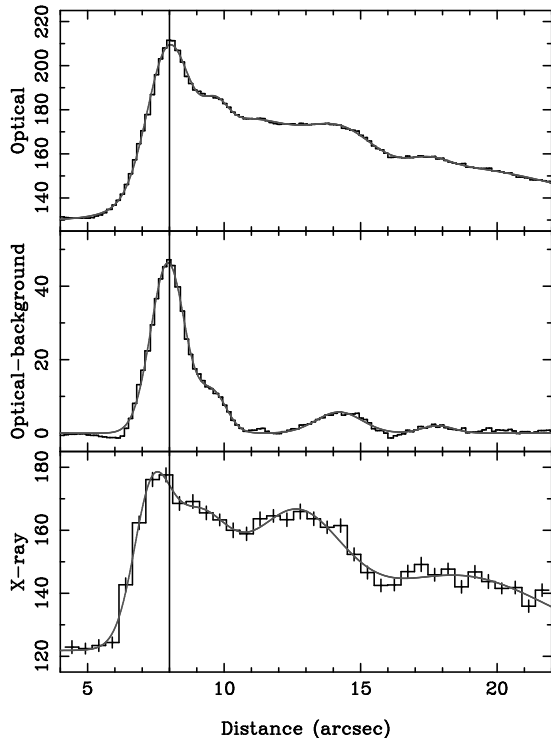


Figure 4. The upper panel shows radial profile of for the average of all the optical observations (in units of $\mu Jy/arcsec^2$). The lower panel shows the average radial profile for all the X-ray data (photon counts) with the exception of ObsIDs 13150 to 13154 to avoid biasing the average due to the concentrated coverage in April 2011 and to maintain a similar sampling cadence as for the optical data. The middle panel repeats the upper panel but with low frequency terms subtracted. The vertical line at $8''$ shows that the brightest and closest optical and X-ray peaks do not exactly coincide.

velocities. These are given in Table 3 where we list the measured quantity i.e. the velocity on the sky in $''/day$, and, assuming a distance of 2 kpc, the physical velocity and the deprojected physical velocity. For deprojection we use an observation angle of $\approx 57^\circ$.

Fig. 6 also compares the motion of the peaks in the radial profiles as a function of time. The figure seems to indicate that each time an X-ray wisp appears close to the pulsar, so does an optical wisp that is slightly further away from the pulsar.

Fig. 7 presents a different yet equally interesting, picture and comparison of the evolution of the peak fluxes in the azimuthal distributions as a function of time. To construct this figure we used a time spacing of 10 days. If an observation took place at any time within the 10 day interval the data were included as a column in the figure. For short gaps in the time sequence, we performed a linear average of the closest columns that contain data. Thus, if there was a two column gap, we would add two thirds of the previous observation to one third of the following observation to fill in the first missing column. For the second missing column,

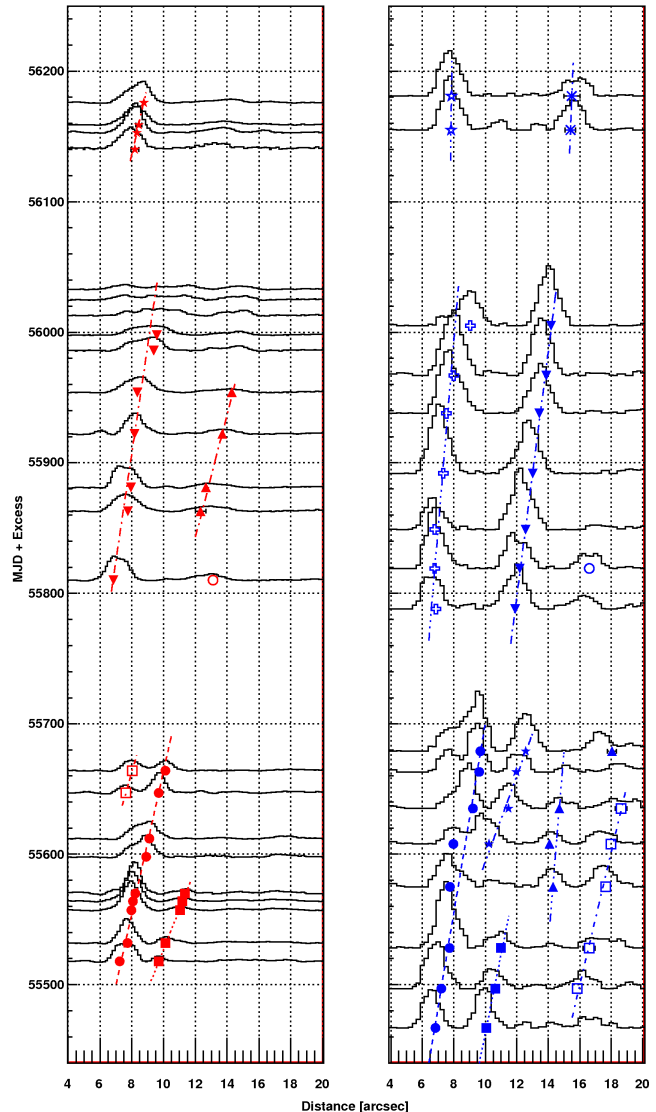


Figure 5. Twenty-three optical and 17 X-ray radial profiles with low-frequency terms removed are plotted as a function of distance northwest of the pulsar. For clarity when one or more observations occur very close in time, we omit them from the figure. The omitted observations are optical - 56140.2 and X-ray - 55665.0, 55665.6, 55667.4, 55673.0, & 56039.1 Symbols are placed on the distance axis to show the position of the peak in the profile. So doing gives the false illusion that the symbols are offset from the peak value. The lines, simply best guesses, are an interpretation of the time evolution of the position of a particular peak.

the weights were reversed. If the wisps in two data sets overlap, this method will cause the wisp to appear to move from the location in the first data set to the location seen in the second across the gap. If the features do not overlap, then features in the first data set will appear to fade as new features appear to grow. We have determined that the gap in the summer break is too long for our interpolation method to work and thus they are empty.

All the features seen in Fig. 5 can also be seen pictorially in Fig. 7. Note that the width of neighboring peaks in the X-ray and optical do not appear to be correlated. In the

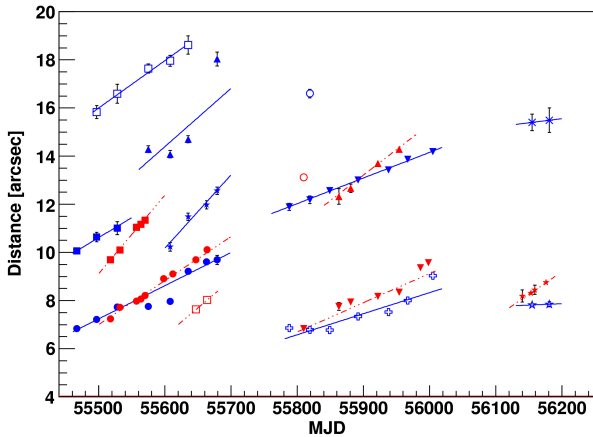


Figure 6. The radial positions of the wisp peaks as a function of time. Red and blue are used to indicate an optical or an X-ray wisp respectively. The symbols are the as in same as in Fig. 5.

X-ray portion of Fig. 7 we also see the slow outward motion of the outer boundary where the color changes from green to blue. This boundary is close to $20''$ from the pulsar for the earliest observations, yet moves to near $25''$ by the end of the sequence. This outward motion of the boundary roughly matches the apparent outward motion of the brighter wisps. Finally, some X-ray peaks do not appear to have nearby optical companion. As a conclusion we can state that the positions of the optical wisps do not align with the positions of the x-ray wisps. That would seem to imply that the individual evolution of optical and X-ray wisps are different. Fig. 7 also makes it clear that new wisps form in the inner region roughly once per year.

3.3 Analysis of the azimuthal profile of the wisps

Good statistics for the optical data allow us to measure the azimuthal intensity profile for each observation. The wisps have an ellipse-like shape in the azimuthal direction around the pulsar, presumably because they are formed in a ring more or less in the equatorial plane of the pulsar. In this case the ellipse-like shape is simply a consequence of projecting a circular ring onto the plane of the sky. In X-rays one finds that the aspect ratio of the innermost ellipse (the location of the presumed termination shock) is 0.49 and the pulsar is displaced along the axis of symmetry by $\approx 0.9''$ below the plane of the ring and along the minor axis which is at a position angle of 110° (Weisskopf et al. 2012). It is more difficult to determine these parameters in the visible primarily because a complete ring is not observed. Nevertheless, averaging all the optical images and assuming this geometrical model, we find a similar offset for the pulsar ($0.8''$) along the spin axis as in X-rays, but with an aspect ratio of 0.6. The different aspect ratio is surely a consequence of our conclusion that the optical and X-ray wisps are not formed in the same regions, with the optical wisps further from the pulsar. Fig. 8 shows the azimuthal distribution of the intensity for two of the optical wisps at distances of $8.0''$ and $10.1''$ from the pulsar. The distributions shown in the figure

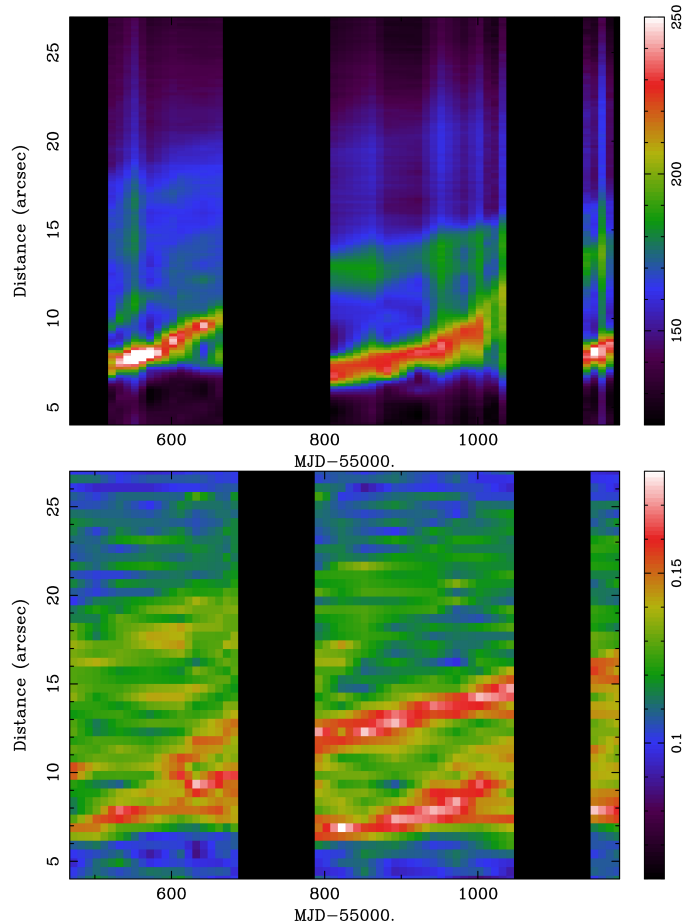


Figure 7. The two panels compare the radial evolution of the optical (upper panel) and X-ray (lower panel) wisps. For clarity, data were interpolated between observations but not across the large gaps imposed by sun constraints.

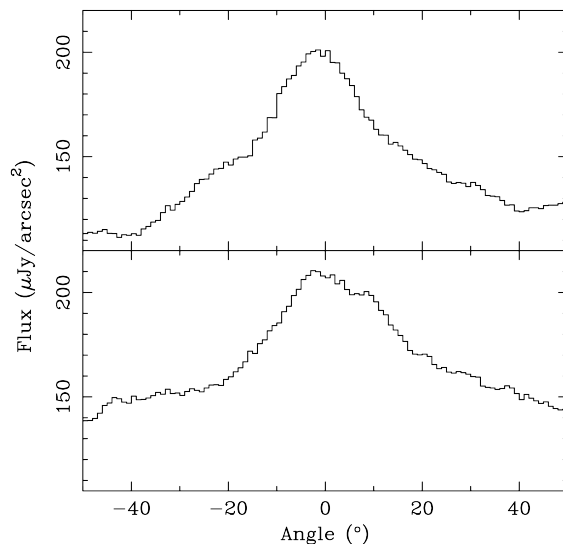


Figure 8. The azimuthal distributions of two optical wisps observed on the 13th of April 2011 at distances of $8.0''$ and $10.1''$ from the pulsar. The angle is the azimuthal angle of the deprojected circle. Zero degrees was set by the peak of the distribution.

was based on a $0.5''$ -wide annulus on an ellipse with the 0.6 aspect ratio.

The X-ray data are noisier than the optical data so we considered both the average of the 2011 April data and the average of all except for the 2011 April data. Within errors, the width of these two distributions were identical. The azimuthal variation in an annulus $0.5''$ wide, $8.0''$ from the pulsar, and centered at the position angle of 119° is shown in Fig. 9. Comparing the X-ray angular distribution with the optical, it is important to note the latter has a sharper peak than that seen in X-rays. The FWHM of the distribution in optical is around 30° while the X-ray distribution has a FWHM of around 70° .

4 MODEL FITTING AND THEORETICAL DISCUSSION

The MHD model developed with success in the past years (Komissarov & Lyubarsky 2003, 2004; Del Zanna et al. 2004; Bucciantini et al. 2005; Del Zanna et al. 2006; Volpi et al. 2008; Camus et al. 2009) explains the existence of rings and wisps observed in pulsar wind nebulae (PWNe) in terms of axisymmetric enhancements of the emissivity immediately downstream of the termination shock. Due to the anisotropy of the pulsar wind luminosity, and the related oblate shape of the termination shock (Del Zanna et al. 2004), axisymmetric regions form inside the nebula where the emissivity toward the observer is higher, either because of local compression of the magnetic field, or because of Doppler boosting. In general it is found that typical flow speeds immediately downstream of the termination shock can be as high as $0.7c$, and the emission is dominated by Doppler boosting.

Komissarov & Lyubarsky (2004) have shown that both the wisps and the knot observed in the Crab Nebula can be qualitatively explained by the geometry of the flow (Fig. 10). In particular the association of the wisps with the wind termination shock is due to the fact that they originate in the flow immediately downstream of the shock itself. A simplified model for a wisp can be built on the assumption that a wisp is due to a torus- or ring-like region within the nebula. This region is bright or dim depending on Doppler boosting due to the relative direction of the observer, and the particle flow. This boosted-ring model appears in alternative explanations for the origin of the wisps, e.g. in term of ion-cyclotron compression (Spitkovsky & Arons 2004) or cooling instabilities (Foy & Hester 2009). The boosting is required in all of these models to explain the azimuthal luminosity profile of the wisps, and the fact that one side of the nebula (the front side) is brighter than the back side. This idea has been adopted in the past (Romani & Ng 2003; Ng & Romani 2004; Romani et al. 2005) to model the jet torus structure observed in X-rays in several PWNe, and to estimate typical flow speeds in these systems.

With reference to Fig. 10, a wisp originates from a region shaped like a torus, with major radius R_o and a minor radius r_o . The ratio r_o/R_o we call the thickness of the torus. The plane of the torus has an inclination α with respect to the line of sight, which, within the axisymmetric approximation, is equal to the angle between the nebular axis and the plane of the sky. The fluid in the torus has a uniform flow speed V_{fl} , confined in meridional planes (planes con-

MJD	Dist	V_{fl}	U_{fl}	$V_{fl,min}$	$V_{fl,max}$	r_o/R_o
55518	5.0	0.87	1.76	0.80	0.92	0.01
55518	7.2	0.96	3.68	0.96	0.97	0.01
55518	8.0	0.95	2.89	0.93	0.96	0.01
55518	9.7	0.80	1.33	0.75	0.85	0.01
55532	7.7	0.94	2.76	0.93	0.95	0.01
55532	10.1	0.83	1.49	0.75	0.87	0.01
55557	8.0	0.94	2.76	0.93	0.95	0.01
55557	10.9	0.90	2.06	0.84	0.93	0.04
55564	8.1	0.95	3.04	0.93	0.96	0.01
55564	11.2	0.92	2.35	0.88	0.96	0.04
55570	8.2	0.95	3.04	0.94	0.96	0.01
55570	11.4	0.92	2.35	0.87	0.94	0.03
55598	8.9	0.94	2.76	0.92	0.95	0.04
55598	11.1	0.90	2.06	0.85	0.92	0.03
55598	12.7	0.70	0.98	0.60	0.85	0.04
55612	8.4	0.93	2.53	0.90	0.95	0.03
55612	9.1	0.93	2.53	0.90	0.94	0.01
55612	11.4	0.80	1.33	0.70	0.87	0.02
55647	7.6	0.97	3.99	0.95	0.98	0.01
55647	9.7	0.97	3.99	0.96	0.98	0.01
55647	12.4	0.90	2.06	0.93	0.85	0.01
55664	5.8	0.85	1.61	0.77	0.91	0.04
55664	8.0	0.93	2.53	0.91	0.95	0.04
55664	10.1	0.91	2.19	0.87	0.93	0.04
55810	6.9	0.93	2.53	0.90	0.95	0.07
55810	12.5	0.93	2.53	0.89	0.96	0.06
55863	5.0	0.80	1.33	0.73	0.90	0.02
55863	7.6	0.93	2.53	0.90	0.95	0.07
55863	12.5	0.93	2.53	0.90	0.95	0.06
55881	7.2	0.95	3.04	0.94	0.96	0.01
55881	8.0	0.94	2.75	0.93	0.95	0.01
55881	10.2	0.80	1.33	0.70	0.87	0.04
55881	12.6	0.90	2.06	0.85	0.93	0.06
55922	6.0	0.86	1.68	0.82	0.90	0.02
55922	8.2	0.93	2.53	0.90	0.97	0.04
55954	8.6	0.90	2.06	0.89	0.93	0.07
55954	12.5	0.90	2.06	0.85	0.95	0.07
55998	9.6	0.92	2.35	0.89	0.95	0.10
56013	7.6	0.93	2.53	0.90	0.95	0.03
56013	8.9	0.92	2.35	0.89	0.94	0.03
56025	7.5	0.94	2.75	0.92	0.97	0.04
56025	9.3	0.90	2.06	0.86	0.92	0.03
56033	7.6	0.94	2.75	0.92	0.97	0.04
56033	9.6	0.87	1.76	0.85	0.89	0.04
56140	8.0	0.95	3.04	0.93	0.96	0.05
56140	13.6	0.85	1.61	0.80	0.88	0.10
56141	8.0	0.95	3.04	0.93	0.96	0.05
56141	13.8	0.80	1.33	0.70	0.85	0.10
56153	8.3	0.96	3.43	0.94	0.97	0.02
56159	8.3	0.95	3.04	0.93	0.96	0.06
56176	8.6	0.95	3.04	0.93	0.96	0.06

Table 4. Fitting parameters for the optical wisps. It lists the MJD, distance to the pulsar, the flow velocity, the boosting four-velocity, and the minimum and maximum flow velocities still compatible with the fit and the thickness of the torus. In all cases we found $\alpha = \beta = 37^\circ \pm 4^\circ$.

taining the nebular axis). The azimuthal component of this flow speed is assumed to be 0. V_{fl} forms an angle β with respect to the plane of the torus.

We want to stress here that V_{fl} is the flow speed of particles in the wisp, and should not be confused with the observed wisp velocity, which we have discussed previously.

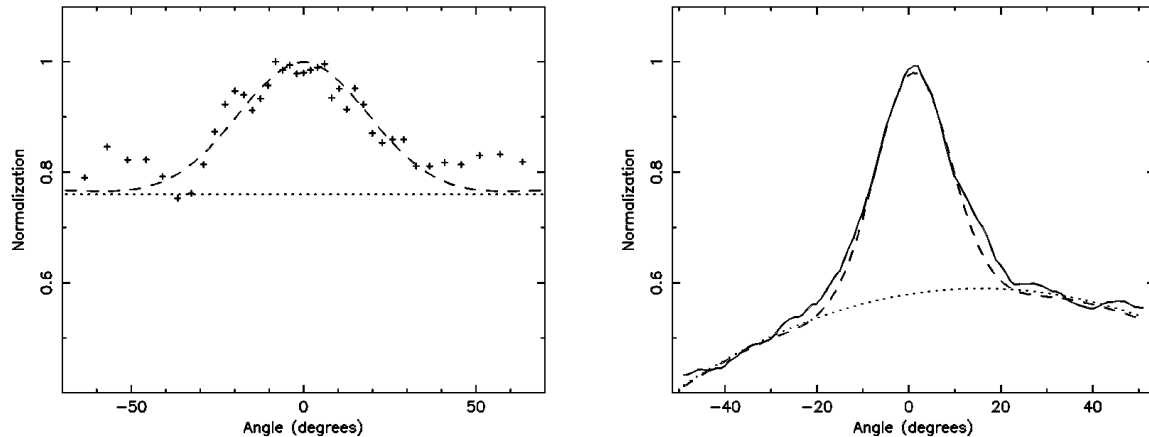


Figure 9. Left panel: The average azimuthal X-ray intensity distribution (normalized to its maximum) in an elliptical annulus at distance of $8''$ to the northwest of the pulsar. The dashed line is a simulated azimuthal distribution as discussed in §4. The dotted line is an assumed background level. Right panel: Same as the left panel but for the average of the optical data nearest the pulsar.

The two are not the same simply because the wisp velocity traces the propagation of the ring in the nebula as a wave, and not the bulk motion of particles. For simplicity we assume uniform synchrotron emissivity inside the torus. In this picture the torus contains a fully ordered toroidal magnetic field, but models can also be built with a chaotic magnetic field (see below for a discussion). The emissivity toward the observer is computed as in previous works (Komissarov & Lyubarsky 2003, 2004; Del Zanna et al. 2004; Bucciantini et al. 2005; Del Zanna et al. 2006; Volpi et al. 2008; Camus et al. 2009) and a synchrotron map is built integrating the contribution of the various parts of the torus along the line of sight. The emitting particles are assumed to be distributed as a power-law in energy with an index -2.35 in agreement with values estimated from optical observations and spectral modeling of the Crab Nebula (Bucciantini et al. 2011). This also applies for the X-ray wisp(s). In the MHD model of PWNe, the wisps are assumed to be located immediately downstream of the termination shock, where particles are accelerated and magnetic field is compressed. Given that the wisps originate from the termination shock, synchrotron cooling should be negligible and the particle distribution unaffected.

The wisps appear brighter northwest of the pulsar and almost fade to the background level in the southeast mostly due to Doppler boosting, given that the flow velocity is generally directed toward the observer in the northwest, while on to the southeast it points away. We want to stress here that the plane of the torus does not necessarily need to coincide (even if it is parallel) with the equatorial plane of the pulsar, but there can be an offset between the two. Such an offset, however, has no consequences in the model for the wisp emissivity.

We fit the optical data to this model as follows:

- We select a set of input parameters r_o/R_o , α , β , and V_{fl} .
- An emission map is built (the emission is normalized to the maximum).

- The emission map is convolved with the point spread function of the observation.
- Emission profiles are extracted both along the wisp and along the axis of the nebula.
- The simulated profiles are compared with the background-subtracted data, both along the axis and along the wisps.
- This procedure is repeated until a set of input parameters are found that provide a reasonable fit. The best fit parameters are obtained by minimizing the residuals in the brightest part of the wisp, where the background subtracted intensity is $> 50\%$ of its maximum value.

The results for the optical wisps are presented in Table 4. We can also roughly quantify the uncertainty in the various parameters. The upper (lower) limit on the flow boosting velocity V_{fl} given in Tab. 4, corresponds to a model which gives a wisp whose FWHM is 15% narrower (larger) than the observed value. Fig. 11 compares one of the optical observations and the result from a simulated map, using the best fit input parameters from Table 4.

We stress here that our procedure does not take into account time-of-flight delays. However, given that the extent of the optical wisps are usually within $\pm 20^\circ$ from the axis, this effect should be negligible.

There are several interesting points to note:

- Typical flow speeds inferred from our model range between $V_{fl} = 0.8c$ and $V_{fl} = 0.95c$. Using a chaotic magnetic field distribution leads to even higher velocities.
- The angle β is almost equal to the angle α .
- The wisps appear to be unresolved and the ratio r_o/R_o is less than 0.1.

The high values of the flow speed correspond to boosting factors that are in excess of typical values found in MHD simulations by about a factor between 2 and 5 depending on which value of β one chooses. This is related to the narrow extent of the optical wisps which fade to the background level within $\pm 20^\circ$ from the axis. This is also connected to the fact that $\beta \approx \alpha$, implying that the flow speed on the front side of the nebula is directed toward the observer. If

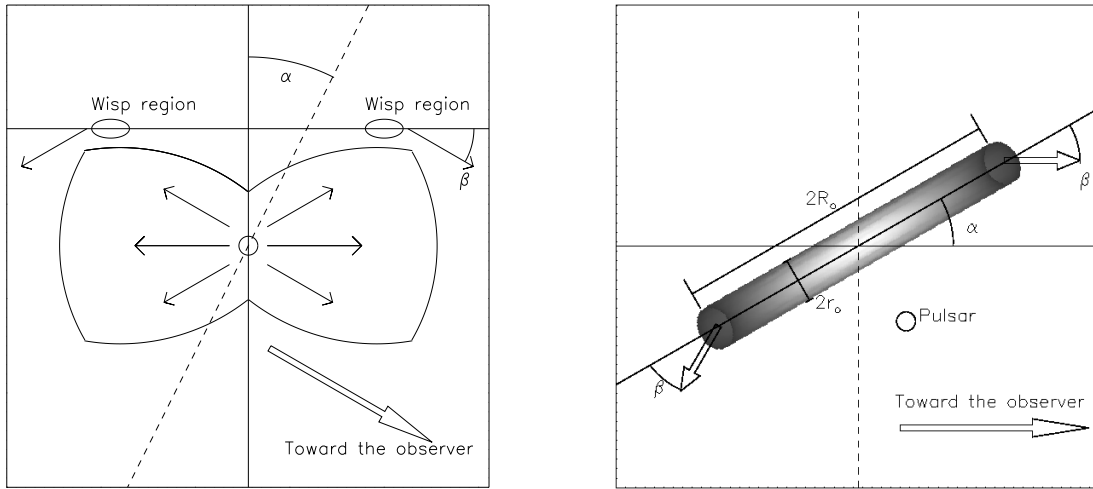


Figure 10. Left panel: Schematic structure of the termination shock and wisps region. The pulsar is located in the central circle from which a relativistic radial wind originates. This wind slows down and is diverted in a termination shock with an oblique shape due to wind anisotropy. The large arrow indicates the direction toward the observer, while the dashed line represents the plane of the sky. The symbol α is the angle between the nebular axis and the plane of the sky and β is the angle between the plane of the wisps and the flow direction in the wisp's regions. Right panel: Schematic of the wisp modeled as an emitting ring. The dashed line is the plane of the sky and R_o and r_o are the major and minor radii of the torus respectively.

β differs from α by more than $3^\circ - 5^\circ$, it is not possible to reproduce the azimuthal wisp luminosity, independently of V_{fl} . The minimum value of V_{fl} is obtained for $\beta = \alpha$. Moreover, it appears that the optical wisps are consistent with narrow features, possibly close to emitting sheets. It is also interesting to note that there is a trend in the observed flow speeds as a function of wisp location, with higher values for inner wisps, as shown in Fig. 12.

A comparison between the azimuthal profile in optical and X-rays has also been done. However, for the X-ray data, in order to have sufficient statistics, instead of a single epoch, we consider first an average over the entire set of observations and only for the inner (brighter) X-ray wisp region located $\sim 8''$ away from the pulsar (Fig. 9). We also repeated this analysis averaging just the 2011 April data with similar results.

The same was done for the optical data, again taking the average over all of our epochs. Results were shown in Fig. 9. The resulting model parameters are $r_o/R_o = 0.1$, $\alpha = \beta = 35^\circ$ both for optical and X-ray, while $V_{fl} = 0.6c \pm 0.1c$ for the X-ray and $V_{fl} = 0.91c \pm 0.03c$ for the optical. We may associate this with a boosting four-velocity $U_{fl} = (V_{fl}/c)/\sqrt{1 - (V_{fl}/c)^2}$ of 0.75 for X-ray and 2.35 for optical (i.e. a factor of 4). Thus, we can safely conclude that the azimuthal extent of this X-ray wisp is larger than in the optical, and consequently the lower inferred speeds in X-ray $\sim 0.5 - 0.7c$ are definitely consistent with expectations from MHD.

The fitting parameters for the optical wisps, however, raise the question if the boosted ring model is in fact appropriate. The MHD model has been developed mostly to reproduce Chandra observations. It is also evident from our study that X-ray and optical wisps are not produced by the

same particle distribution: they do not coincide in location or in terms of the degree of Doppler boosting.

It is not our intention here develop and provide an alternative explanation for the azimuthal luminosity of the optical wisps, but we can point to a few possible solutions:

- Optical wisps appear to originate in the transition layer at the termination shock itself. This is consistent with the thin-sheet hypothesis and the idea that, at the shock itself, the flow speed is higher than in the downstream region. It remains to be proven that the geometry of the shock can allow for such configurations.
- Emissivity is enhanced along the axis of the nebula because of local clumpiness. Clumps are observed in X-rays, called by some *sprites*, and they have a more or less stable location. However, why in optical, these clumps should be located along the axis of the nebula is not clear.
- If the particle distribution in a wisp is non-isotropic, then the emissivity has a stronger dependence on the inclination of the magnetic field with respect to the line of sight than in the isotropic case. It is not clear, however, what the degree of anisotropy needs to be and if it can be produced by known acceleration mechanisms.

5 CONCLUSION

We find that approximately once per year optical and X-ray wisps appear and peel off from the region commonly associated with the termination shock of the pulsar wind. Moreover, the X-ray and optical wisps are physically separated. Interestingly enough, the time interval for γ -ray flares is also about 1 year leading to the speculation that the flaring may

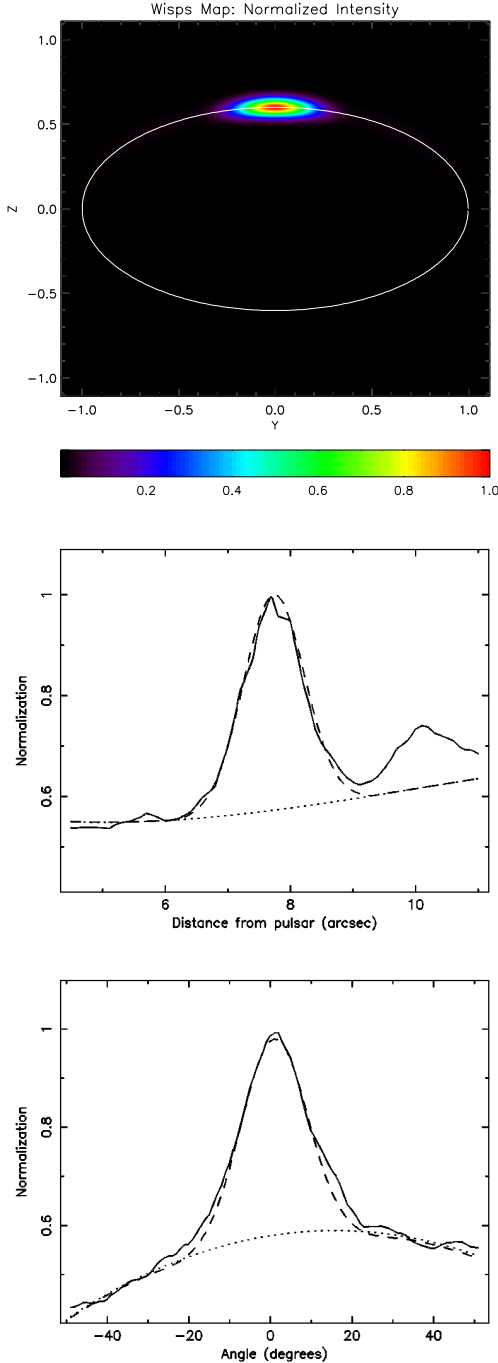


Figure 11. Upper panel: Simulated synchrotron map of the optical wisp for MJD=55532 and at a distance of $7.7''$ derived using the fitting parameters in Tab. 4. The axes are in arbitrary units normalized to the wisp major radius R_o . Colors indicate the level of the flux, normalized to the maximum. Middle panel: the solid line is the optical profile of the wisp along the nebular axis, while the dashed line is obtained from the simulated synchrotron map. The dotted line is the (assumed) background. Lower panel: Same as the middle panel but for the azimuthal profile.

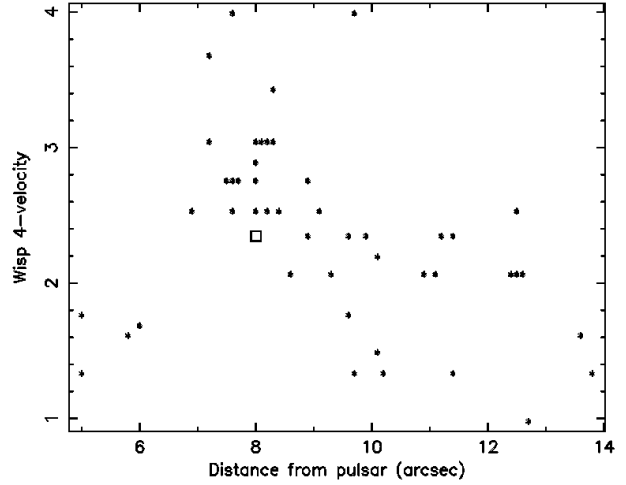


Figure 12. Boosting four-velocity $(V_{fl}/c)/\sqrt{1 - (V_{fl}/c)^2}$ for the optical wisps as a function of their distance from the pulsar. The square denotes the boosting four-velocity obtained from the averaged optical profile. Note that the data points at radii $\leq 7''$ are most likely not due to wisps, but other optical features such as the halo (Hester 2008).

somehow be associated with wisp formation. However, since the wisps did not form in coincidence with the γ -ray flare of 2011 April which took place during this study, the speculation requires a theory that has the formation of the wisps substantially (\approx month) preceding a γ -ray flare.

These wisps propagate outward with velocities projected onto the sky ranging from $0.1(v/c)$ to $0.4(v/c)$ (Table 3). If anything, there appears to be a trend for the projected velocity of a wisp increasing, the further it is from the pulsar, perhaps implying a re-acceleration mechanism. More likely, this apparent behavior may be a result of the more complicated three-dimensional geometry and there may be no need for re-acceleration when properly deprojected. Another word of caution is that one might be confusing optical features in the counter-jet with structure in the wisps.

Within the context of an MHD model, we also find that optical wisps are more strongly Doppler-boosted than the X-ray wisps. In particular, we found that the azimuthal luminosity profile of the X-ray wisps is fully compatible with typical boosting factors found in MHD simulations of PWNe. Instead, the azimuthal luminosity profile of the optical wisps requires particles velocities that are incompatible with the results of global numerical modeling of PWNe (Komissarov & Lyubarsky 2003; Bucciantini et al. 2005). It is also interesting to note that the optical wisps as well as the X-ray wisps are Doppler boosted in the direction of the observer, which implies that the movement of particles has a component in the direction of the observer. This may be simply an accident or due to a selection effect as we tend to observe high-flux regions and the Doppler boosting enhances the flux. This should be investigated with future modeling.

ACKNOWLEDGMENTS

The optical observations used in this work have been done with the Nordic Optical Telescope, operated on the island of La Palma jointly by Denmark, Finland, Iceland, Norway and Sweden, in the Spanish Observatorio del Roque de los Muchachos of the Instituto de Astrofísica de Canarias. The data were obtained [in part] with ALFOSC, which is provided by the Instituto de Astrofísica de Andalucía (IAA) under a joint agreement with the University of Copenhagen and NOTSA. The staff at the NOT provided much useful support, particularly Thomas Augusteijn.

The X-ray observations have been done with the Chandra X-ray satellite. A.T. and M.C.W would like to acknowledge support from the Chandra Project. We would also like to acknowledge the Director of the Chandra Science Center for authorizing Director's Discretionary Time and Chandra Proposal 1350025 for the remainder of the observations.

REFERENCES

- Abdo A. A., Ackermann M., Ajello M., Allafort A., Baldini L., Ballet J., et al. 2011, *Science*, 331, 739
- Bietenholz M. F., Hester J. J., Frail D. A., Bartel N., 2004, *ApJ*, 615, 794
- Bucciantini N., Arons J., Amato E., 2011, *MNRAS*, 410, 381
- Bucciantini N., del Zanna L., Amato E., Volpi D., 2005, *A&A*, 443, 519
- Buehler R., Scargle J. D., Blandford R. D., Baldini L., Baring M. G. e. a., 2012, *ApJ*, 749, 8
- Camus N. F., Komissarov S. S., Bucciantini N., Hughes P. A., 2009, *MNRAS*, 400, 1241
- Del Zanna L., Amato E., Bucciantini N., 2004, *A&A*, 421, 1063
- Del Zanna L., Volpi D., Amato E., Bucciantini N., 2006, *A&A*, 453, 621
- Foy J. P., Hester J., 2009, in *American Astronomical Society Meeting Abstracts #213 Vol. 41 of Bulletin of the American Astronomical Society, The Effect of Synchrotron Cooling on the Structure of the Crab Nebula*. p. 488.01
- Hester J. J., 2008, *ARA&A*, 46, 127
- Hester J. J., Mori K., Burrows D., Gallagher J. S., Graham J. R., Halverson M. e. a., 2002, *ApJ*, 577, L49
- Hester J. J., Scowen P. A., Sankrit R., Burrows C. J., Gallagher III J. S., Holtzman J. A., Watson A., et al. 1995, *ApJ*, 448, 240
- Komissarov S. S., Lyubarsky Y. E., 2003, *MNRAS*, 344, L93
- Komissarov S. S., Lyubarsky Y. E., 2004, *MNRAS*, 349, 779
- Li J., Kastner J. H., Prigozhin G. Y., Schulz N. S., Feigelson E. D., Getman K. V., 2004, *ApJ*, 610, 9
- Morhác M., Kliman J., Matoušek V., Veselský M., Turzo I., 1997, *Nuclear Instruments and Methods in Physics Research A*, 401, 113
- Ng C.-Y., Romani R. W., 2004, *ApJ*, 601, 479
- Romani R. W., Ng C.-Y., 2003, *ApJ*, 585, L41
- Romani R. W., Ng C.-Y., Dodson R., Briskin W., 2005, *ApJ*, 631, 480
- Sandberg A., Sollerman J., 2009, *A&A*, 504, 525
- Scargle J. D., 1969, *ApJ*, 156, 401
- Spitkovsky A., Arons J., 2004, *ApJ*, 603, 669
- Tavani M., Bulgarelli A., Vittorini V., Pellizzoni A., Striani E., Caraveo P., Weisskopf M. C., Tennant A., et al. 2011, *Science*, 331, 736
- Volpi D., Del Zanna L., Amato E., Bucciantini N., 2008, *A&A*, 485, 337
- Weisskopf M. C., Elsner R. F., Kolodziejczak J. J., O'Dell S. L., Tennant A. F., 2012, *ApJ*, 746, 41